Dynamics of a non-linear Jeffcott rotor in supercritical regime

Roberto Alcorta, Benjamin Chouvion, Olivier Montagnier

Dynamics of a non-linear Jeffcott rotor in supercritical regime

Roberto Alcorta[a,*], Benjamin Chouvion[a], Olivier Montagnier[a]

[a]*Centre de Recherche de l'Ecole de l'air (CREA), Ecole de l'air et de l'espace, 13661 Salon-de-Provence, France*

Abstract

This work is concerned with the prediction and simulation of limit cycles of a nonlinear Jeffcott rotor. Geometrical nonlinearity (related to large flexural displacements) in both stiffness and internal damping is considered. Classical instabilities due to linear internal damping occurring in the supercritical range are modified by nonlinear effects and lead to oscillating limit cycles at a radius whose value is found analytically as a function of the rotating speed. If the rotor is additionally excited by unbalance, the response spectrum also contains the excitation frequency, and the bifurcation leads to quasi-periodic limit cycles. The dynamics of this system is studied numerically via the harmonic balance method, path continuation and bifurcation tracking. In particular, an original procedure for switching to a branch of quasi-periodic solutions is proposed. To preserve the integrity of the machine post bifurcation, one then considers the possibility of constraining the transverse displacement of the shaft. Such possible rotor stator interaction generates three-frequency quasi-periodic oscillations. Frequency response curves show that the quasi-periodic solutions created by the bouncing rotor are mainly driven by the friction coefficient.

Keywords: Bifurcation tracking, Branch switching, Geometrical nonlinearities, Quasi-periodic solutions, Rotor stator contact

1. Introduction

The Jeffcott rotor (or Laval rotor) is a reference case useful to understand essential phenomena in rotordynamics. It is well known that linear analysis of a Jeffcott rotor with internal damping leads to unstable forward modes in the supercritical regime (rotating nominal speed higher than first critical speed) [1, 2]. This instability can cause fatal damage to the rotor. It is one of the reasons why engineers avoid the supercritical regime, for instance on helicopter rear drive shafts. However, in that case, letting the rotor turn in this

*Corresponding author
Email address: roberto.alcorta@ecole-air.fr (Roberto Alcorta)

regime has been shown to allow for increased shaft lengths and reduced number of supports, consequently reducing maintenance costs [3, 4]. Moreover, rotor shafts with pinned end conditions are also subjected to nonlinear geometric effects due to mid-plane stretching. As these are only prominent for large-amplitude motions, they are often ignored in rotordynamics models. Nevertheless, they are important for ensuring bounded amplitudes in the case of linearly unstable regimes. Genta [5] conducted a thorough analytical and numerical study of a nonlinear rotor with 'Duffing-like' cubic stiffness, and deduced conditions for stable circular whirling. Recently, two frequency quasi-periodic cycles were reported in the unbalance response of a simple Jeffcott rotor with nonlinear damping [6] in the supercritical regime. If these kinds of high amplitude modes appear in this regime, for example with a sudden increase in the unbalance of the shaft due to an impact, one way of preserving the integrity of the rotor could be to constrain the transverse displacement of the shaft with a static ring or stator.

Rubbing between the rotor and stator can be found in many applications, ranging from turbomachine designs where the gap between blades and stator is so narrow that abradable wear removal is now seriously considered [7] to drill string systems in which the extremely long rotating part with flexible joints will inevitably generate interaction between the drill string and an outer shell [8]. In particular, Chipato et al. have demonstrated friction plays a major role in shaping the dynamics of unbalanced, overhung rotors through numerical [9] and experimental [10] means. Their results show different quasi-periodic bouncing regimes, whose frequency content is interpreted in relation to the rotor's forward and backward whirl frequencies, and which in some cases require the presence of friction to exist.

It stands to reason that rotors designed to operate at high rotation speeds will be subjected to a combination of the aforementioned phenomena, which are often considered individually in the literature. Hence, this contribution deals with the study of a supercritical, nonlinear Jeffcott rotor with possible rotor stator interaction. A shaft with pinned ends is considered, whose large transverse displacements provide both a nonlinear stiffness and a nonlinear internal damping. The corresponding equations of motion are consistently derived from an energetic approach and then approximated to the third order to obtain a Duffing-type oscillator with two degrees of freedom. Furthermore, rotor stator interactions are introduced as a penalty formulation of contact with Coulomb friction [11]. The detailed mathematical description of the rotor model is given in Sect. 2 and numerical tools employed for its simulation are detailed in Sect. 3. These include, in particular, an original procedure to switch from periodic to quasi-periodic branches at a Neimark-Sacker bifurcation. The case of a balanced, unconstrained rotor is first presented in Sect. 4. Either beyond stability or near the resonant frequency of the rotor excited by an unbalanced mass, the structure can undergo transverse dis-

placement such that it makes contact with the surrounding stator. The study of the full system and its limit cycles, including unbalance and contact, is the subject of Sect. 5. The presence of the dissipative friction force at the rotor-stator interface leads to complex nonlinear phenomena with the creation of a quasi-periodic regime. This paper focuses on the simulation and understanding of such strongly nonlinear behavior. The consistent incorporation of nonlinear effects into the rotor model, along with the use of Neimark-Sacker bifurcation tracking to explore the parameter space, are additional novelties of the present work.

2. Nonlinear Jeffcott rotor model

The structural model is based on the classical Jeffcott rotor [2] on top of which geometrical nonlinearities and possible rotor stator contact are considered, see Fig. 1.

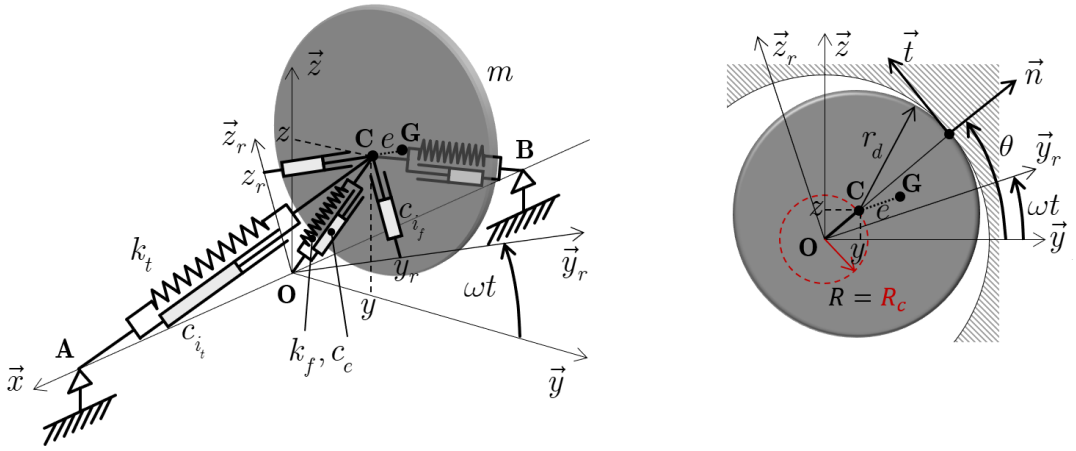

Figure 1: Jeffcott rotor with large transverse displacement, pinned-ends, and possible rotor stator interaction

2.1. Equations of motion of the unconstrained rotor

The structure studied consists of an unbalanced disk mounted on a massless, axisymmetric shaft. The disk is modeled as a lumped mass m in G located at a distance e from the centre of rotation C (see Fig. 1). Without gravity forces and without rotation, the centre of rotation is located in O. The disk inertia in the axial direction is noted I. The rotating frame linked to the disk $(\mathrm{O},\vec{y}_r,\vec{z}_r)$ turns relatively to the fixed frame $(\mathrm{O},\vec{y},\vec{z})$ with a rotating speed ω. The length of the shaft is l. Its stiffness and internal viscous damping corresponding to flexural (transverse) movement are denoted k_f and c_{i_f}. In case of large displacement, shaft stiffening related to membrane tension effects is accounted for with a constant stiffness equal to k_t for

the half-length. Internal viscous damping is also considered in that direction, along the shaft length, and is denoted c_{i_t}. An important source of external dissipation in rotordynamics applications is the viscoelastic material upon which shaft bearings are mounted. Several studies model this effect in a precise way, e.g. [3, 4], but this requires considering additional degrees of freedom for bearing displacements. Instead, for modelling convenience, here the supports are assumed to constrain the displacements in the radial and transversal directions but to dissipate radially with a viscous damping coefficient c_e. Contact forces from possible rotor stator interaction are also accounted for. These exist if the structure transversal displacement is large enough to nullify the initial gap present on the undeformed configuration. The kinetic energy of the system can be written in the following form (with the time derivative $\dot{\circ} = d\circ/dt$):

$$T = \frac{1}{2}m\left(\dot{y}^2 + \dot{z}^2 + e^2\omega^2 - 2e\dot{y}\omega\sin(\omega t) + 2e\dot{z}\omega\cos(\omega t)\right) + \frac{1}{2}I\omega^2, \tag{1}$$

where y and z are coordinates of the centre of rotation C in the fixed frame. The potential energy from internal and external forces is equal to:

$$U = \frac{1}{2}k_f\left(y^2 + z^2\right) + \frac{1}{4}k_t\left(\sqrt{l^2 + 4y^2 + 4z^2} - l\right)^2 + mg\left(y + e\sin(\omega t)\right) + U^c_{cons}. \tag{2}$$

In Eq. (2), the geometric nonlinear effects are simply obtained with the Pythagorean theorem, and the term U^c_{cons} represents the potential associated with conservative contact forces. Naturally, a beam model in large displacements and rotations would be needed to accurately quantify the geometric nonlinearity due to shaft deflection. However to stay in the framework of a Jeffcott rotor, the qualitative picture obtained by replacing the shaft by springs is deemed sufficient. The global dissipation expression, which includes external and internal viscous dampers, and dissipation due to friction through the term $\mathscr{D}^c_{diss}$, can be written as:

$$\mathscr{D} = \frac{1}{2}c_e\left(\dot{y}^2 + \dot{z}^2\right) + \frac{1}{2}c_{i_f}\left((\dot{y} + \omega z)^2 + (\dot{z} - \omega y)^2\right) + \frac{1}{4}c_{i_t}\frac{(y\dot{y} + z\dot{z})^2}{l^2 + 4y^2 + 4z^2} + \mathscr{D}^c_{diss}. \tag{3}$$

The term in c_{i_t} of Eq. (3) was obtained noting that the internal structural dissipation along the shaft length is proportional to the velocity of C in the frame related to the rotating disk and not in the fixed frame [1]. The internal dissipation on the AC segment, equal to the one on the BC segment, is then proportional to the square of the velocity of C in the AC direction. This gives a dissipation term equal to $2\frac{1}{2}c_{i_t}\left(\vec{v_C}\cdot\vec{AC}/||\vec{AC}||\right)^2$ where $\vec{v_C}$ is the velocity of C.

Governing equations are derived from Lagrange's equations using the energies and dissipation function

defined in Eqs. (1), (3) and (2). These become:

$$\ddot{y}+(d_e+d_{i_f})\dot{y}+\omega_f^2 y+d_{i_f}\omega z+\frac{1}{2}d_{i_t}\frac{y^2\dot{y}+yz\dot{z}}{l^2+4y^2+4z^2}+\omega_t^2\left(1-\frac{l}{\sqrt{l^2+4y^2+4z^2}}\right)y = e\omega^2\cos(\omega t)-f_y^c, \quad (4a)$$

$$\ddot{z}+(d_e+d_{i_f})\dot{z}+\omega_f^2 z-d_{i_f}\omega y+\frac{1}{2}d_{i_t}\frac{yz\dot{y}+z^2\dot{z}}{l^2+4y^2+4z^2}+\omega_t^2\left(1-\frac{l}{\sqrt{l^2+4y^2+4z^2}}\right)z = e\omega^2\sin(\omega t)+g-f_z^c, \quad (4b)$$

where $d_e=c_e/m$, $d_{i_f}=c_{i_f}/m$, $d_{i_t}=c_{i_t}/m$, $\omega_f=\sqrt{k_f/m}$ and $\omega_t=\sqrt{2k_t/m}$ denote respectively the external modal damping, the internal modal damping, the natural frequency of the undamped shaft in bending and the natural frequency of the undamped shaft in tension. It is relatively straightforward to verify that the nonlinear damping expressed in Eq. (4), like classical internal damping, dissipates no energy during precession or purely circular motions. Contact forces, generically given by $f_q^c=\partial U_{cons}^c/\partial q+\partial \mathscr{D}_{diss}^c/\partial\dot{q}$, $q=\{y,z\}$, will be detailed in Sect. 2.2. Eq. (4) is then rewritten by approximating the geometric nonlinear term by their Taylor expansion truncated at third order, and using a non-dimensional form obtained by appropriately scaling lengths and time. The governing equations of motion become:

$$Y''+(D_e+D_{i_f})Y'+Y+D_{i_f}\Omega Z+Y\left[D_{i_t}\left(YY'+ZZ'\right)+2\Omega_t^2(Y^2+Z^2)\right]+F_Y^c=E\Omega^2\cos(\Omega\tau), \quad (5a)$$

$$Z''+(D_e+D_{i_f})Z'+Z-D_{i_f}\Omega Y+Z\left[D_{i_t}\left(YY'+ZZ'\right)+2\Omega_t^2(Y^2+Z^2)\right]+F_Z^c=E\Omega^2\sin(\Omega\tau)+G. \quad (5b)$$

with

$$Y=\frac{y}{l},\quad Z=\frac{z}{l},\quad D_e=\frac{d_e}{\omega_f},\quad D_{i_f}=\frac{d_{i_f}}{\omega_f},\quad D_{i_t}=\frac{d_{i_t}}{2\omega_f},\quad F_q^c=\frac{f_q^c}{l\omega_f^2}$$
$$\Omega=\frac{\omega}{\omega_f},\quad \Omega_t=\frac{\omega_t}{\omega_f},\quad E=\frac{e}{l},\quad \tau=\omega_f t,\quad G=\frac{g}{l\omega_f^2},$$

and $(.)'=\dot{(.)}/\omega_f=d(.)/d\tau$. It shall be noted that, due to possible contact with the stator, transversal amplitudes are severely limited. Hence, the smallness assumption is duly justified in this context and a third-order approximation of geometric terms is consistent.

2.2. Contact model

The terms F_Y^c and F_Z^c in Eqs. (5a) and (5b) are the components of the reaction force at the contact point, resolved in fixed-frame coordinates. Considering a circular stator with radius R_c, those are defined with:

$$\mathbf{F}^c(Y,Z,Y',Z') = \begin{bmatrix} F_Y^c \\ F_Y^c \end{bmatrix} = \frac{1}{R}\hat{H}(R-R_c)\begin{bmatrix} F_N Y - F_T Z \\ F_N Z + F_T Y \end{bmatrix}, \tag{6}$$

where $R = \sqrt{Y^2+Z^2}$ is the disk's (non-dimensional) radial displacement and $\hat{H}$ is the Heaviside function, indicating non-zero forces for $R \geq R_c$ only. The scalar functions F_N and F_T denote, respectively, the force components in the normal and tangential directions to the stator circumference at the contact point. Here, F_N is defined by the penalty law:

$$F_N = \Omega_c^2(R-R_c). \tag{7}$$

The distance $R-R_c$ may be interpreted as disk penetration into the stator or as a measure of elastic deformation of the former due to contact. The term $\Omega_c = \omega_c/\omega_f$, where $\omega_c = \sqrt{k_c/m}$, serves as a non-dimensional penalty coefficient associated to the contact stiffness k_c. The tangential force, F_T, is a result of friction, and thus can be modelled in a number of ways [12]. In this paper, a simple Coulomb (dry friction) law is used:

$$F_T = \mu|F_N|\text{sign}(v_r), \tag{8}$$

where $v_r = v_t + \Omega\frac{r_d}{l}$ is the (non-dimensional) velocity between rotor and stator at the contact point, including contributions from the former's elastic motion (v_t) and rotation about its axis ($\Omega\frac{r_d}{l}$), with r_d being the disk radius), and μ is the dry friction coefficient. One may remark that, in the fixed frame: $v_t = (YZ'-ZY')/R = \theta' R$, where $\theta = \arctan(Z/Y)$ is the disk's angular displacement. Moreover, the absolute value can be omitted from the above equation in light of Eqs. (6) and (7).

3. Numerical methods

In order to solve Eq. (5) and perform parametric studies, numerical continuation based on the Harmonic Balance Method (HBM) is used. This section briefly describes this approach.

Let $\mathbf{X} = [Y,Z]^T$ and rewrite Eq. (5) as a single vector equation, i.e.:

$$\mathbf{X}'' + \mathbf{C}\mathbf{X}' + \mathbf{X} + \mathbf{F}_{\text{NL}}(\mathbf{X},\mathbf{X}',\Omega) = E\Omega^2\mathbf{F}_e(\tau) + \mathbf{G}, \tag{9}$$

where $\mathbf{F}_e(\tau) = [\cos\Omega\tau, \sin\Omega\tau]^T$, $\mathbf{G} = [0,G]^T$, the diagonal matrix $\mathbf{C}$ contains $D_e + D_{i_f}$ in its diagonal, and all remaining terms are grouped into vector $\mathbf{F}_{\text{NL}}$. Then, the steady-state solution of (9) is approximated by a

periodic solution and sought by expanding each term as a Fourier series truncated at the N_h-th harmonic, i.e.

$$\mathbf{X}(\tau) = \sum_{k=0}^{N_h} \left\{ \hat{\mathbf{X}}_{ck} \cos k\hat{\Omega}\tau + \hat{\mathbf{X}}_{sk} \sin k\hat{\Omega}\tau \right\}. \tag{10}$$

Replacing this Fourier expansion into Eq. (9), and balancing terms with the same harmonic yields to the following non-linear algebraic system for the Fourier coefficients

$$\hat{\mathbf{X}} = \left[\hat{\mathbf{X}}_0, \hat{\mathbf{X}}_{c1}, \hat{\mathbf{X}}_{s1}, ..., \hat{\mathbf{X}}_{cN_h}, \hat{\mathbf{X}}_{sN_h} \right] :$$

$$\mathbf{R}(\hat{\mathbf{X}}) = \mathbf{Z}(\hat{\Omega})\hat{\mathbf{X}} + \hat{\mathbf{F}}_{\mathbf{NL}}(\hat{\mathbf{X}}, \hat{\Omega}) - E\Omega^2 \hat{\mathbf{F}}_e - \hat{\mathbf{G}} = \mathbf{0}, \tag{11}$$

in which $\mathbf{Z}(\hat{\Omega}) = \hat{\Omega}^2(\nabla^2 \otimes \mathbf{I}_2) + \hat{\Omega}\nabla \otimes \mathbf{C} + \mathbf{I}_{2(2N_h+1)}$ is the dynamic stiffness matrix. The notation $\hat{\Omega}$ above is used to distinguish between the forced (unbalanced) and free (balanced) cases: in the former, the whirling frequency is equal to the rotor angular speed, so that $\hat{\Omega} = \Omega$; in the latter, $\hat{\Omega}$ is not known a priori and must be computed along with $\hat{\mathbf{X}}$. Thus, the free case requires appending an additional equation to Eq. (11); this is done in such a way to fix the cycle phase, which is otherwise undetermined for autonomous systems [13]. In the frequency domain, this takes the simple form: $\mathbf{v}_{ph}^T \hat{\mathbf{X}} = 0$, with $\mathbf{v}_{ph}$ a well-chosen constant vector. The skew-symmetric operator ∇ maps the Fourier coefficients of $\hat{\mathbf{X}}$ to those of its time derivative. In the following numerical simulations, the state-dependent term $\hat{\mathbf{F}}_{\mathrm{NL}}$, that relates to the harmonic coefficients of the non-linear force, is computed with the Alternating Frequency-Time method (AFT) [14], after which Eq. (11) lends itself to a solution through Newton-Raphson iterations. Furthermore, a full response curve is constructed by an arc-length continuation algorithm which includes local stability and bifurcation analysis for each converged solution. The main difficulties are detailed next.

3.1. Stability and bifurcation tracking

Following [11], a small perturbation $\mathbf{p}(\tau)$ is applied to a periodic solution $\mathbf{X}_{sol}(\tau)$ of Eq. (9) such that $\mathbf{X}(\tau) = \mathbf{X}_{sol}(\tau) + \mathbf{p}(\tau)$. This allows to linearize the aforementioned equation around $\mathbf{X}_{sol}(\tau)$, which yields a periodic-coefficient system for $\mathbf{p}(\tau)$. From Floquet theory, this system admits 4 linearly independent solutions of the form: $\mathbf{p}_j(\tau) = \varphi_j(\tau) e^{\lambda_j \tau}$ for $j = \{1, ..., 4\}$, where the vector functions $\varphi_j(\tau)$ are periodic. Applying the HBM then leads to the following quadratic eigenvalue problem for the characteristic (Floquet) exponents λ_j and their corresponding frequency-domain eigenvectors, Φ_j:

$$\left[\lambda_j^2 \mathbf{I}_{2(2H+1)} + \lambda_j \mathbf{D}_1 + \mathbf{R}_{\hat{\mathbf{X}}} \right] \Phi_j = \mathbf{0}, \tag{12}$$

where

$$\mathbf{D}_1 = 2\hat{\Omega}(\nabla \otimes \mathbf{I}_2) + \mathbb{F}\left\{ \partial \mathbf{F}_{\mathbf{NL}} / \partial \mathbf{X}' \right\} (\nabla \otimes \mathbf{I}_2) + \mathbf{I}_{2H+1} \otimes \mathbf{C} \quad \text{and} \quad \mathbf{R}_{\hat{\mathbf{X}}} = \partial \mathbf{R} / \partial \hat{\mathbf{X}}.$$

The condition $\forall j,\ \Re\left\{\lambda_j\right\} < 0$ characterizes a stable cycle, as it describes a perturbation decaying over time regardless of how said perturbation is applied. As the system's parameters vary, one of more Floquet exponents are amenable to crossing the imaginary axis. A case of particular interest is the Neimark-Sacker (NS) bifurcation, defined by the existence of a pure imaginary exponent pair: $\lambda_{1,2} = \pm i\eta$, which gives birth to a branch of quasi-periodic solutions. Stability changes are detected along solution branches by monitoring $\Re\left\{\lambda_j\right\}$. Critical values are pinpointed by using Newton iterations to solve the following extended system characterizing a NS bifurcation [15]:

$$\begin{bmatrix} \mathbf{R} \\ (\mathbf{R}_{\hat{\mathbf{X}}} - \eta^2 \mathbf{I}_{2(2H+1)})\Phi_R - \eta \mathbf{D}_1 \Phi_I \\ (\mathbf{R}_{\hat{\mathbf{X}}} - \eta^2 \mathbf{I}_{2(2H+1)})\Phi_I + \eta \mathbf{D}_1 \Phi_R \\ N_1(\Phi_R, \Phi_I) \\ N_2(\Phi_R, \Phi_I) \end{bmatrix} = \mathbf{0}, \tag{13}$$

where Φ_R and Φ_I are the real and imaginary parts of the unstable eigenvectors $\Phi_{1,2}$, such that $\Phi_{1,2} = \Phi_R \pm \mathrm{i}\Phi_I$, uniquely defined through the scalar normalization conditions N_1 and N_2. Solving Eq. (13) for any continuation parameter α yields to specific values (noted with subscript $_{\mathrm{NS}}$) describing the system at the NS bifurcation point. These are the harmonic coefficient (noted $\hat{\mathbf{X}}_{\mathrm{NS}}$) of the degrees of freedom related to the physical displacement with an inverse Fourier transform, the eigenvector (real Φ_R, and imaginary Φ_I parts), the additional frequency created by the bifurcation (η_{NS}), and the continuation parameter (α_{NS}). In the free case, a phase condition must be included in Eq. (13) to solve for the whirling frequency $\hat{\Omega}_{\mathrm{NS}}$. From an initial solution, continuation can be applied to Eq. (13), thus tracking NS bifurcations in two arbitrary parameters α and β.

3.2. Branch switching to quasi-periodic solutions

In order to switch between two periodic branches at a bifurcation point, a well-known method exists in which the tangent vector to the emerging branch is directly computed by making use of a quadratic equation [13]. This approach was recently applied in combination with the HBM, for instance in [16, 17, 18]. Alternatively, the parallel search methodology explained in [19] can be used to find a solution on the new branch without explicitly computing the associated tangent vector. This section presents a procedure for branch switching at a NS bifurcation inspired by parallel search, thus allowing to find an initial quasi-periodic solution on an emerging branch. The key idea is that a branching point corresponds to a certain symmetry breaking in the system, which is also reflected in the frequency-domain representation. Hence,

if the Fourier coefficient vector of periodic solutions is partitioned into two mutually orthogonal parts, say a 'symmetric' (noted $\hat{\mathbf{X}}_s$) and an 'antisymmetric' (noted $\hat{\mathbf{X}}_a$) one, i.e.: $\hat{\mathbf{X}} = \hat{\mathbf{X}}_s + \hat{\mathbf{X}}_a$ such that $\hat{\mathbf{X}}_s^T \hat{\mathbf{X}}_a = 0$, all solutions on the main branch satisfy $\hat{\mathbf{X}}_a = \mathbf{0}$ whereas this is not the case for solutions on the emerging branch. Typical examples of partitions are: even and odd harmonics, and Fourier coefficients of individual degrees of freedom. For instance, the even/odd harmonic decomposition of a Fourier coefficient vector with $N_h = 2$ simply reads:

$$\hat{\mathbf{X}} = \begin{bmatrix} \hat{\mathbf{X}}_0 \\ \hat{\mathbf{X}}_{c1} \\ \hat{\mathbf{X}}_{s1} \\ \hat{\mathbf{X}}_{c2} \\ \hat{\mathbf{X}}_{s2} \end{bmatrix} \Longrightarrow \hat{\mathbf{X}}_s = \begin{bmatrix} \hat{\mathbf{X}}_0 \\ \hat{\mathbf{X}}_{c1} \\ \hat{\mathbf{X}}_{s1} \\ \mathbf{0} \\ \mathbf{0} \end{bmatrix} \quad \text{and} \quad \hat{\mathbf{X}}_a = \begin{bmatrix} \mathbf{0} \\ \mathbf{0} \\ \mathbf{0} \\ \hat{\mathbf{X}}_{c2} \\ \hat{\mathbf{X}}_{s2} \end{bmatrix}.$$

Clearly, a tangent vector to the emerging branch at the bifurcation point must be a linear combination of a tangent vector to the main branch at the same point, $\mathbf{t}_s$, and a second one belonging to a subspace spanned by $\hat{\mathbf{X}}_a$. A good candidate for the latter (see, e.g., [13]) is the eigenvector Φ associated to the unstable eigenvalue characterizing the bifurcation. The parallel search algorithm consists in finding a solution by first taking a step along Φ at the bifurcation point and then performing Newton-Raphson corrections along the direction of $\mathbf{t}_s$.

In order to extend this idea to NS bifurcations, let us consider the expression of a quasi-periodic solution using a two-dimensional hyper-time approach [20], in which the time scales $\theta_1 = \hat{\Omega}\tau$ and $\theta_2 = \eta\tau$ are introduced in place of proper time τ within Eq. (9). The displacement is then defined by the following two-dimensional Fourier series:

$$\mathbf{X}(\tau) = \sum_{a=-N_h}^{N_h} \sum_{b=0}^{N_h} \hat{\mathbf{X}}_{c(a,b)} \cos(a\hat{\Omega} + b\eta)\tau + \hat{\mathbf{X}}_{s(a,b)} \sin(a\hat{\Omega} + b\eta)\tau. \tag{14}$$

It is worth noting that a full description of a quasi-periodic solution requires only one of the above sums to cover negative values of the summing index, due to the fact that the signals we consider (displacement time histories) are real [21]. Periodic solutions, which were expressed before as a simple Fourier series (see Eq. (10)), may be seen as a particular case of the above equation (i.e. with $b = 0$). By introducing Eq. (14) into Eq. (9) and balancing harmonics, the following algebraic system is obtained:

$$\mathbf{R}(\hat{\mathbf{X}}, \hat{\Omega}, \eta) = \mathbf{Z}(\hat{\Omega}, \eta)\hat{\mathbf{X}} + \hat{\mathbf{F}}_{\mathrm{NL}}(\hat{\mathbf{X}}, \hat{\Omega}) - E\Omega^2 \hat{\mathbf{F}}_e - \hat{\mathbf{G}} = \mathbf{0}, \tag{15}$$

which differs from Eq. (11) in two crucial ways. Firstly, the dynamic stiffness matrix becomes: $\mathbf{Z}(\hat{\Omega}, \eta) =$

$\hat{\nabla}^2 \otimes \mathbf{I}_2 + \hat{\nabla} \otimes \mathbf{C} + \mathbf{I}_{2(2N_h+1)}$ with the new differential operator $\hat{\nabla} = \hat{\Omega}\nabla_1 + \eta\nabla_2$. In turn, the linear operators ∇_1 and ∇_2 represent frequency-domain partial derivatives associated with time scales θ_1 and θ_2, respectively. Secondly, computation of the term $\hat{\mathbf{F}}_{\mathrm{NL}}$ now requires to use two-dimensional Fourier transforms in the AFT procedure.

The general quasi-periodic solution (14) is next partitioned into a 'periodic part', containing all coefficients associated with the first frequency (i.e. $b = 0$) and a second part containing the remaining coefficients ($b \neq 0$). These are represented by the vectors $\hat{\mathbf{X}}_{\mathrm{P}}$ and $\hat{\mathbf{X}}_{\mathrm{QP}}$, respectively. Then, for instance, a periodic solution expressed in the extended basis reads:

$$\hat{\mathbf{X}} = \begin{bmatrix} \hat{\mathbf{X}}_{\mathrm{P}} \\ \hat{\mathbf{X}}_{\mathrm{QP}} \end{bmatrix} = \begin{bmatrix} \hat{\mathbf{X}}_{\mathrm{P}} \\ \mathbf{0} \end{bmatrix},$$

in which $\hat{\mathbf{X}}_{\mathrm{P}}$ contains the subset of coefficients where $a \neq 0$ and $b = 0$. In particular, this is the form of $\mathbf{t}_p$, the tangent vector to the periodic branch at a bifurcation point. This offers a very natural way of partitioning, and thus a NS bifurcation may be treated as a classical branching point. From the explanation given in Sect. 3.1, a perturbation applied in the direction of the unstable eigenvector at the NS point evolves in time as:

$$\mathbf{p}(\tau) = e^{\mathrm{i}\eta\tau}\mathbb{F}^{-1}\left[\Phi_R + \mathrm{i}\Phi_I\right] + e^{-\mathrm{i}\eta t}\mathbb{F}^{-1}\left[\Phi_R - \mathrm{i}\Phi_I\right] = 2\left[\cos(\eta\tau)\varphi_R(\hat{\Omega}\tau) - \sin(\eta\tau)\varphi_I(\hat{\Omega}\tau)\right], \tag{16}$$

where $\mathbb{F}^{-1}(\cdot)$ denotes the inverse one-dimensional Fourier transform, producing the purely periodic functions $\varphi_R(\hat{\Omega}\tau)$ and $\varphi_I(\hat{\Omega}\tau)$ from the real and imaginary parts, respectively, of the unstable eigenvector computed through Eq. (13). From Eq. 16, a straightforward computation shows that the spectrum of $\mathbf{p}(\tau)$ consists of terms associated with the basis functions $\left[\cos(a\hat{\Omega}+\eta), \sin(a\hat{\Omega}+\eta)\right]$ where $a \in \{-N_h, ..., N_h\}$. Thus, if we let $\mathbf{t}_{\mathrm{NS}}$ denote the Fourier coefficient vector of $\mathbf{p}(\tau)$ in the extended basis, it follows that $\mathbf{t}_{\mathrm{NS}}$ and $\mathbf{t}_p$ are mutually orthogonal. Consequently, the unit vector tangent to the emerging branch at the NS bifurcation is a combination of both $\mathbf{t}_p$ and $\mathbf{t}_{\mathrm{NS}}$, which completes the setting for parallel search.

As a final remark before introducing the branching algorithm, let note that the second frequency η has been introduced into the system of equations, which is now under-determined and must be closed by an additional equation. In a manner analogous to periodic solutions of autonomous systems, this indeterminacy is a consequence of the initial phase with respect to time-scale θ_2 not being imposed by the forcing terms. One might arbitrarily choose the phase condition: $(\partial Y/\partial\theta_2)|_{\tau=0} = 0$, which is readily expressed in the frequency domain as: $\mathbf{v}_{ph}^T\hat{\mathbf{X}} = 0$, where $\mathbf{v}_{ph}^T$ is a constant vector.

In summary, the procedure to switch branches at a NS bifurcation during continuation is as follows:

1. Localize a NS point by solving Eq. (13).
2. Compute $\mathbf{t}_p$ and $\mathbf{t}_{\mathrm{NS}}$, then express them both in the extended Fourier basis along with $\hat{\mathbf{X}}_{\mathrm{NS}}$.
3. Taking the values $(\hat{\mathbf{X}}_{\mathrm{NS}} + \varepsilon \mathbf{t}_{\mathrm{NS}}, \alpha_{\mathrm{NS}}, \eta_{\mathrm{NS}})$ for small $\varepsilon \in \mathbb{R}$ as a starting point, use Newton-Raphson iterations in a direction parallel to $\mathbf{t}_p$, i.e. with corrections given by:

$$\begin{bmatrix} \mathbf{R}_{\hat{\mathbf{X}}} & \mathbf{R}_\alpha & \mathbf{R}_\eta \\ \mathbf{v}_{ph} & 0 & 0 \\ \mathbf{t}_{\mathrm{NS}} & 0 & 0 \end{bmatrix} \begin{bmatrix} \delta\hat{\mathbf{X}} \\ \delta\alpha \\ \delta\eta \end{bmatrix} = - \begin{bmatrix} \mathbf{R} \\ \mathbf{v}_{ph}^T \hat{\mathbf{X}} \\ 0 \end{bmatrix}. \tag{17}$$

   where the residual vector $\mathbf{R}$ and its derivatives correspond to Eq. (15).
4. After successful convergence to a quasi-periodic solution, use standard arc-length continuation to follow the newly obtained branch. The phase condition is kept, while the last line of (17) is replaced by an arc-length equation.

Whereas the tool presented in Sect. 3.1 is used to detect bifurcation points and assess the stability of the branch being scanned with the continuation procedure, the method explained in Sect. 3.2 can be used to initiate the path following on a detected branch of quasi-periodic solutions. Overall, the methodology ensures that all steady-state solutions obtainable for varying α are captured by the continuation algorithm.

4. Unconstrained system

This section focuses on the solution of the unconstrained (unbounded) rotor. Of particular interest is the vibrational state existing at high rotating speed, after a supercritical bifurcation. A closed-form expression is found to describe the limit cycles in the free case in Sect. 4.1. Sect. 4.2 presents numerical simulations investigating in more details the post-bifurcation regime in both the free and forced cases.

4.1. Analytical solution

Free vibrations (balanced rotor, i.e., $E = 0$) are first considered and the effect of gravity terms and contact are neglected. Fixed points, noted $\bar{\mathbf{X}} = [\bar{Y}, \bar{Z}]^T$, of the system are obtained solving Eq. (5) with $\dot{\bar{\mathbf{X}}} = \mathbf{0}$. This gives:

$$\begin{cases} \bar{Y} + D_{i_f}\Omega\bar{Z} + 2\Omega_t^2(\bar{Y}^2 + \bar{Z}^2)\bar{Y} = 0 \\ \bar{Z} - D_{i_f}\Omega\bar{Y} + 2\Omega_t^2(\bar{Y}^2 + \bar{Z}^2)\bar{Z} = 0 \end{cases} \tag{18}$$

whose single fixed point solution is $\bar{\mathbf{X}}_0 = [0,0]^T$. The local stability of this fixed point is then assessed by complex eigenvalue analysis of Eq. (18) linearized around $\bar{\mathbf{X}}_0$. In this case, the closed-form expression of the eigenvalues becomes:

$$\lambda_{1,\dots,4} = \frac{1}{2}\left(-(D_e + D_{i_f}) \pm 2\sqrt{-\Omega_d^2 \pm \mathrm{i} D_{i_f}\Omega}\right), \tag{19}$$

where

$$\Omega_d^2 = 1 - \frac{1}{4}(D_e + D_{i_f})^2. \tag{20}$$

The expansion of the complex square root is useful to separate the damping part (real part) from the frequency (imaginary part) of the exponents. One then obtains two exponents and their associated complex conjugates:

$$\lambda_{1,2} = -A + B \pm \mathrm{i}C \quad \text{and} \quad \lambda_{3,4} = -A - B \pm \mathrm{i}C, \tag{21}$$

with

$$A = \frac{1}{2}(D_e + D_{i_f}), \quad B = \frac{1}{\sqrt{2}}\sqrt{-\Omega_d^2 + \sqrt{\Omega_d^4 + D_{i_f}^2\Omega^2}} \quad \text{and} \quad C = \frac{1}{\sqrt{2}}\sqrt{\Omega_d^2 + \sqrt{\Omega_d^4 + D_{i_f}^2\Omega^2}}.$$

These eigenvalues are generally given in an approximate form [1]. Modes 3 and 4 are unconditionally stable because $\Re(\lambda_{3,4}) < 0\ \forall\Omega$. The others can become unstable with sufficiently large Ω. Indeed, $\Re(\lambda_{1,2}) > 0$ if the rotating frequency is larger than the critical speed Ω_{HB} given by:

$$\Omega_{\mathrm{HB}} = 1 + \frac{D_e}{D_{i_f}}. \tag{22}$$

When $\Omega = \Omega_{\mathrm{HB}}$, The dynamical system is at a Hopf bifurcation point defined with two complex conjugate eigenvalues having real parts changing sign [13]. Consequently, a branch of periodic solutions (limit cycles) emerges from this point. The remaining of this section is devoted in finding an exact analytical solution for these limit cycles. Using $R = Y + \mathrm{i}Z$, the previous system (namely, Eq. (18)) can be reformulated in the form of a single complex equation, as in [5]:

$$R'' + (D_e + D_{i_f})R' + \left(1 - \mathrm{i}D_{i_f}\Omega\right)R + \frac{1}{2}D_{i_t}\left(|R|^2R' + R^2\bar{R}'\right) + 2\Omega_t^2|R|^2R = 0. \tag{23}$$

The limit cycle solution is sought after in the following form: $R = |R|\mathrm{e}^{\mathrm{i}\bar{\Omega}t}$, where the unknowns $|R|$ and $\bar{\Omega}$ are respectively the circle radius and rotating speed of the periodic cycle. Substituting this form into Eq. (23) gives:

$$\left(-\bar{\Omega}^2 + (D_e + D_{i_f})\mathrm{i}\bar{\Omega} + (1 - \mathrm{i}D_{i_f}\Omega + 2\Omega_t^2|R|^2\right)|R|\mathrm{e}^{\mathrm{i}\bar{\Omega}t} = 0. \tag{24}$$

This equation is not affected by nonlinear internal dissipation simply because $|R|^2R' + R^2\bar{R}' = 0$. With $\Omega > 1$ (condition respected after the Hopf bifurcation, see (22)), the following non-trivial solution of (24) can be found:

$$\begin{cases} \bar{\Omega} = \dfrac{D_{i_f}}{D_e + D_{i_f}}\Omega = \dfrac{\Omega}{\Omega_{\mathrm{HB}}} \\ |R| = \dfrac{1}{\sqrt{2}\Omega_t}\sqrt{\bar{\Omega}^2 - 1} \end{cases} . \tag{25}$$

This solution (25) defines the oscillating limit cycle. From bifurcation theory, this branch of solution is stable while the fixed point $\bar{\mathbf{X}} = \mathbf{0}$ is unstable. The evolution of the rotating speed of the limit cycle is linear relatively to Ω. When $\bar{\Omega}$ gets larger, $|R| \to \bar{\Omega}/(\sqrt{2}\Omega_t)$ and the evolution of the cycle radius tends also to be linear relatively to Ω. Finally, it can be remarked that this solution is not written in a *normal form* [13] because the problem is here solved directly in the physical space and not on an approximated invariant manifold.

4.2. Parametric study

Let consider the case of a homogeneous elastic shaft with circular cross section of external radius r and Young modulus E_a. Its stiffness in tension and in bending are respectively equal to $k_t = E_a S/l = E_a \pi r^2/l$ and $k_f = 48E_a I/l^3 = 12E_a \pi r^4/l^3$. The ratio between the tension and bending natural frequencies is $\Omega_t = l/(\sqrt{6}r)$. With $r = 1\,\mathrm{cm}$ and $l = 1.2\,\mathrm{m}$, its order of magnitude is $\Omega_t \approx 50$. According to [3], let use $D_e = D_{i_f} = 0.1$, which yields to a Hopf bifurcation at $\Omega_{\mathrm{HB}} = 2$, see Eq. (22). Figure 2 illustrates time history of the rotor dynamical behaviour for different initial positions and at $\Omega = 5$, calculated with numerical time integration. These converge towards a limit cycle of radius approximately 0.0331, consistent with the analytical solution given in Eq. (25).

The Hopf bifurcation and the limit cycle can also be obtained numerically via a continuation procedure following the explanations given in Sect. 3. This is illustrated in Fig. 3 that shows that the amplitude of the limit cycles is exactly evaluated by the analytical solution Eq. (25).

Investigating the analytical solution (22) and (25) more deeply can give insights on the behaviour of the limit cycle as a function of the system configuration. For instance, one can easily show that the cycle radius is inversely proportional to the ratio l/r for a given Ω, which means that long shaft will tend to have smaller cycle limit amplitude. The classical behaviour of a Jeffcott rotor with respect to damping [1] is also confirmed by (25): external damping has a beneficial effect by delaying the appearance of the limit cycles whereas internal damping has a destabilizing effect. It is finally worth noticing that a small D_e/D_{i_f} ratio leads to a low bifurcation frequency ($\Omega_{\mathrm{HB}} \to 1$ for $D_e/D_{i_f} \to 0$) and high limit cycle amplitude. In practical

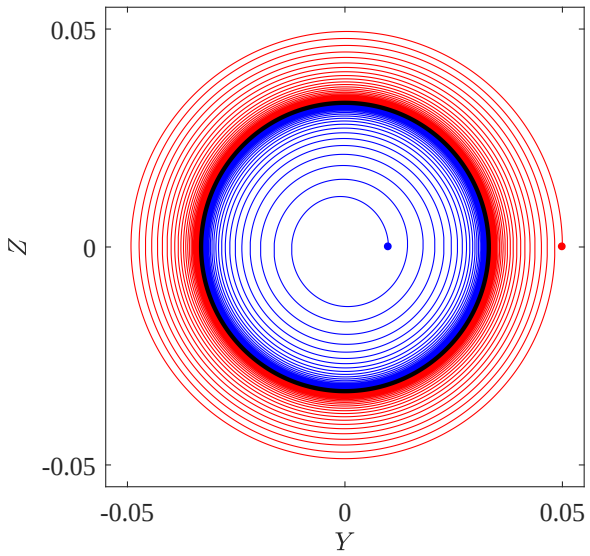

Figure 2: Temporal simulation of rotor past Hopf bifurcation point, highlighting the limit cycle. Red (——) and blue (——) trajectories start from initial conditions $(Y_0, \dot{Y}_0, Z_0, \dot{Z}_0) = (0.05, 0, 0, 0.18)$ and $(Y_0, \dot{Y}_0, Z_0, \dot{Z}_0) = (0.01, 0, 0, 0.013)$

, respectively, and converge to black (- - -) cycle with radius $|R| = 0.033$.

applications of supercritical shafts with low D_e/D_{i_f} ratio, the rotating damping instability can then appear but not be differentiated with an oscillating forced response due to unbalance. The two of them could be distinguished looking at the phase of the response because the limit cycle speed is different from the rotating speed. Simulations of an unbalanced rotor are performed next.

Fig. 4 shows the radial amplitude of an nonlinear unbalanced rotor with $E = 5.0 \times 10^{-4}$. The main branch of solution is periodic (labelled 'P' in Fig. 4) due to the periodic forcing (see Eq. (5)) created by the unbalance mass. It was obtained through numerical continuation as per Sect. 3, with $H = 5$. Because of the relatively small value chosen for E, the characteristic turning points near resonance of Duffing-like oscillators are absent from this figure; nevertheless, visual evidence of the system's nonlinear nature lies in the asymmetrical peak shape at $\Omega \approx 1$ and in the slight shift of the effective resonant frequency due to stress stiffening. On the other hand, a branch of stable quasi-periodic solutions emerges from a supercritical NS bifurcation at $\Omega_{\text{NS}} = 2.03$. This value is remarkably close to the analytical Hopf bifurcation speed $(\Omega_{\text{HB}} = 2)$ of the balanced rotor. Having localized the bifurcation, parallel-search branch-switching as described in Sect. 3.2 is applied with $\varepsilon = 10^{-4}$. A first quasi-periodic solution is thus obtained in few

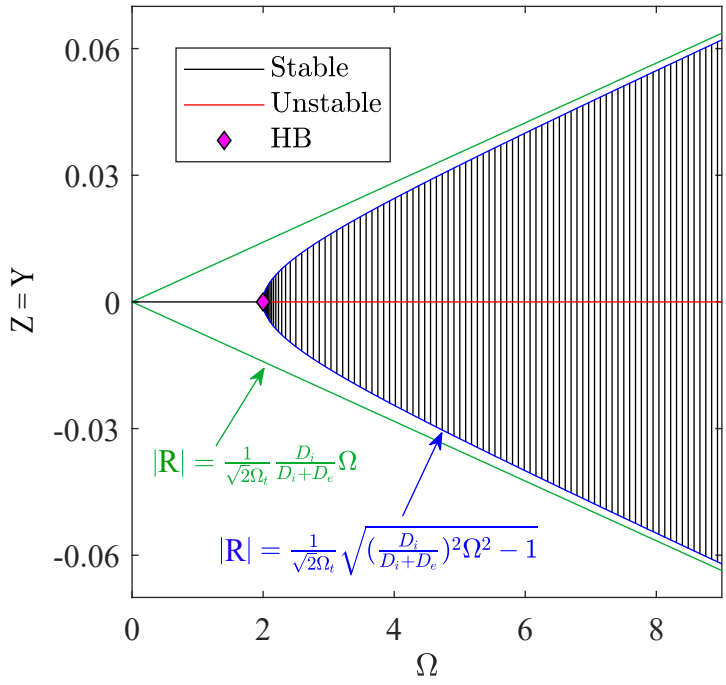

Figure 3: Hopf bifurcation and limit cycles of the system obtained with continuation of Eq. (5) without applied forces – Comparison with analytical solution (25).

iterations, allowing the whole branch (denoted QP in Fig. 4) to be computed via continuation. Results from numerical time integration shown in Fig.4 directly performed on Eq. (4) confirmed both the third-order Taylor approximation of the nonlinear forces and the harmonic truncation in the Fourier expansion of the HBM. Another illustration of such results is shown in Fig. 5, where $\Omega = 2.5$ was fixed. At this value, the only stable attractor is the quasi-periodic solution on the upper branch of Fig 4.

Fig. 5.a) shows the steady-state rotor trajectory in fixed-frame coordinates (Y,Z). The quasi-periodic response to unbalance manifests as a torus centred about the underlying limit cycle, which is also shown for comparison. Indeed, as seen in Fig. 5.b), the radial displacement $R(\tau) = \sqrt{Y^2+Z^2}$ is constant on the circular orbit described by the latter, whereas it oscillates periodically for the former. Consequently, the power spectra obtained from a Fourier Transform of these signals (i.e. Fig. 5.c)) exhibits a main peak at zero frequency, with an additional peak corresponding to the second frequency $\eta = 1.2487 = \Omega_{\text{HB}}$ in the unbalanced case. Just as for the balanced rotor, this whirling has its origin in rotating damping. This

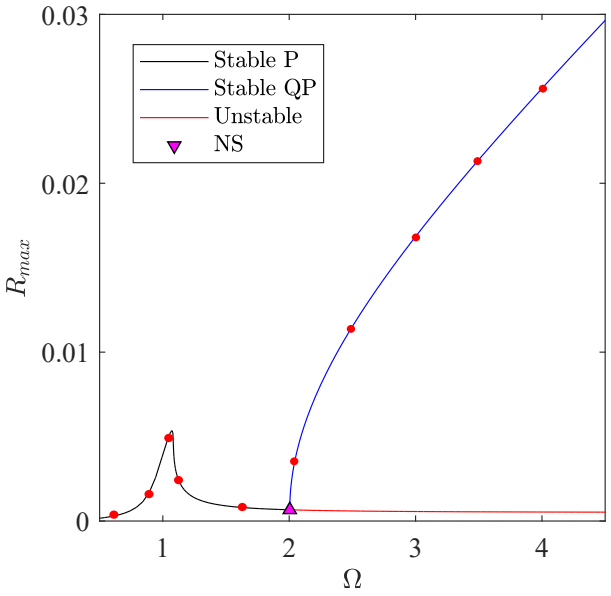

Figure 4: Radial amplitude of the unbalance response of unconstrained rotor ($E = 5.0 \times 10^{-4}$). Markers (●) show time integration results.

motion is superimposed to the unbalance response, resulting in a net quasi-periodic motion since $\Omega/\eta \notin \mathbb{Q}$. The remaining apparent peaks in the balanced case spectrum are small and due exclusively to numerical approximations; hence, they are not relevant.

To better understand the global dynamics of the system, the evolution of its forced response for varying E is investigated. The results are encapsulated in Figs. 6 and 7. The former of these presents four curves, computed for the values $E = [5,\ 7.5,\ 10,\ 12.5] \times 10^{-4}$ over the interval $\Omega \in [0.5, 3.0]$, the first of which coincides with Fig. 4. The effect of nonlinear stiffness is clearly seen around the resonant velocity $\Omega = 1$ for increased E, as evidenced by the appearance of an unstable branch bordered by Limit Point (LP) bifurcations. This behaviour is typical of hardening ($\Omega_t^2 > 0$) nonlinearities of the cubic type. At these simulated response amplitude levels, the solutions obtained from the full and approximated models are indistinguishable. Nevertheless, the amplitude of the resonant peak increases rapidly with the mass eccentricity. This can be seen immediately by tracking LP bifurcations – as presented in this figure – and entails two consequences: from a computational perspective, the third-order approximation becomes inaccurate to evaluate the high-level LP; physically, the rotor is prone to reaching critical amplitudes if the transverse displacement

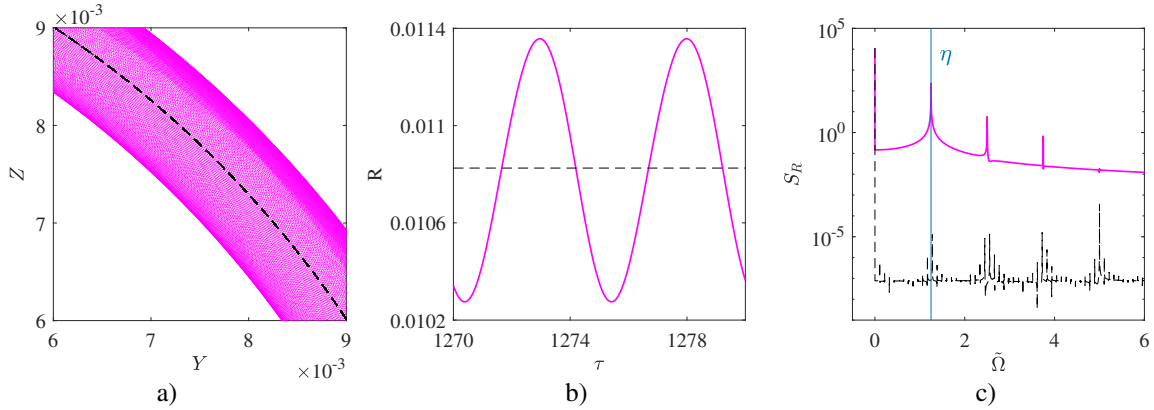

Figure 5: Rotor response at fixed frequency $\Omega = 2.5$ (no contact): a) rotor trajectory, and b) time history $R(\tau)$, and c) power spectra of radial displacement (noted S_R). Forced and free responses are represented by solid magenta (——) and dashed black (- - -) lines, respectively.

of the rotor is not mechanically constrained. It is important to realize that this event arrives well before the maximum allowable value $E = r_d/l = 8.33 \times 10^{-3}$. If one assumes that only the approximate maximum amplitude of the response near resonance is of interest and that the system is with light damping, one could have followed the $\pi/2$ phase change occurring at resonance in the (E,Ω) space, as performed in [22]. This alternative approach has the advantage of being easier to implement numerically than tracking the upper LP (see Fig. 6).

With regard to the NS bifurcations leading to quasi-periodic motions, they occur at higher rotating speeds for increased values of E. As the mass eccentricity tends to zero, $\Omega_{\mathrm{NS}} \to \Omega_{\mathrm{HB}}$. Fig. 7, which consists of a projection of the bifurcation curves on the (Ω,E) plane, evidences this fact. Another interesting aspect that surfaces from this figure is that, whenever $E > 1.229 \times 10^{-3}$, there exists a region where stable periodic and quasi-periodic solutions co-exist. On this projection, such a region is made up of points simultaneously to the right of the NS boundary and within the cusp defined by the LP boundary.

Taking the point labelled **A** (see Figs. 6 and 7), corresponding to $(\Omega,E) = (2.08, 1.25E-3)$, as an example, the steady-state solution eventually reached depends on initial conditions, see Fig. 8. Finally, the LP curve includes a cusp point (labelled CSP in Fig. 7) located at $(\Omega,E) = (1.09, 5.31 \times 10^{-4})$; this defines a minimal value of eccentricity beyond which an unstable branch will exist on the main resonance peak.

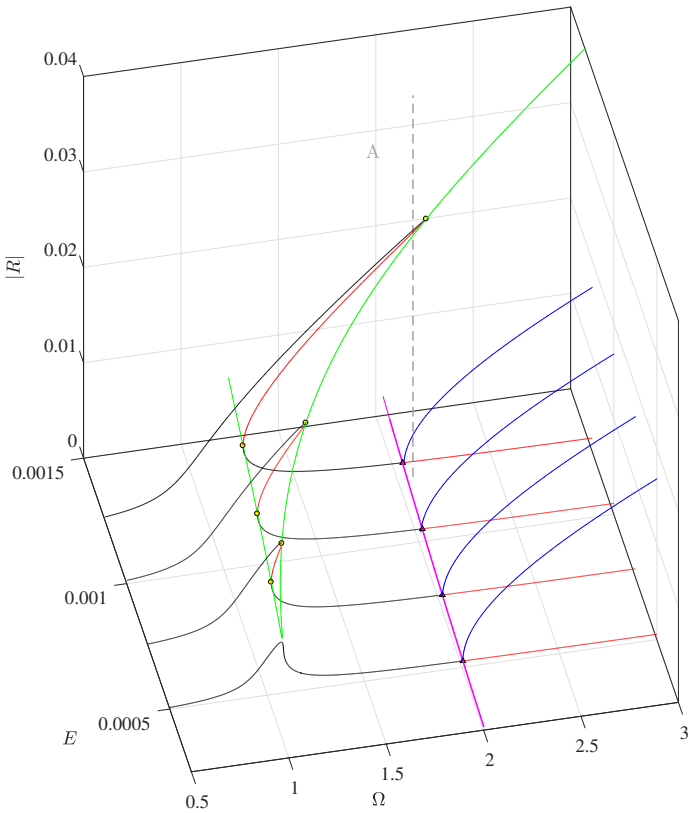

Figure 6: Response curves of unbalanced rotor for varying E. Also shown are stability boundaries for LP and NS bifurcations. The vertical line at $(\Omega, E) = (2.08, 1.25 \times 10^{-3})$, labelled **A**, indicates an example of co-existing, stable periodic and quasi-periodic solutions.

5. Constrained rotor

In this section, the response of balanced and unbalanced rotors in the presence of a circular stator is studied. The stator can bound the transverse displacement of the shaft when subjected to external resonance or high-oscillating limit cycles and is located at the radial distance $r_d + R_c$ with $R_c = 0.0175$. The contact parameters are initially fixed at: $\mu = 0.3$ and $\Omega_c^2 = 50$ (see Sect. 2.2 for details on the contact model). The numerical value for the friction coefficient μ is inspired by the value $\mu = 0.35$ experimentally measured by Chiapato et al. [10].

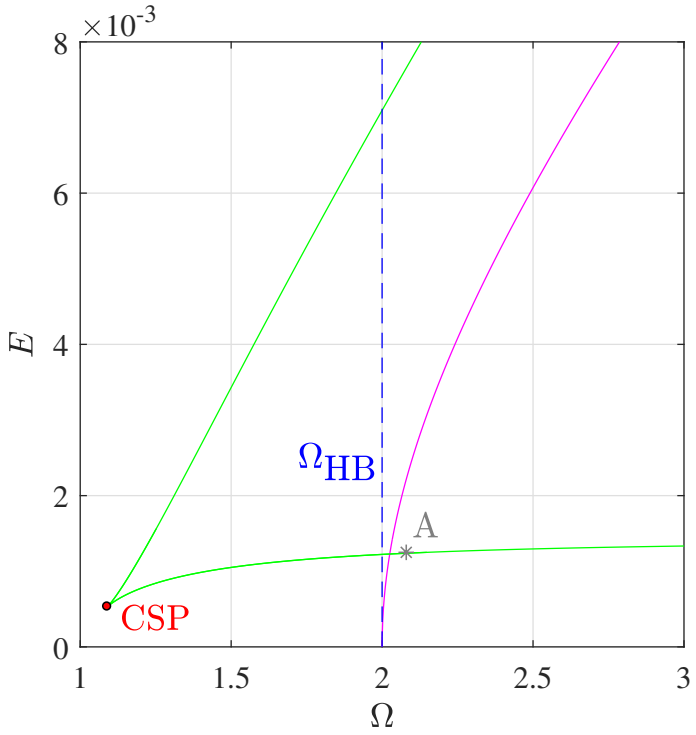

Figure 7: Bifurcation boundaries in (Ω, E) plane: LP (——) and NS (——).

5.1. Frequency response

The balanced rotor's response for varying Ω is presented in Fig. 9. An abrupt slope change as R attains R_c clearly indicates the onset of contact. Due to the penalty formulation employed, cycle amplitudes beyond R_c are allowed but penetrations remain small even for the moderate value of Ω_c^2 used herein. A NS bifurcation occurs immediately after $R = R_c$, so that all periodic solutions beyond this point are unstable. Quasi-periodic motions then develop, a behaviour which agrees with reported results on rubbing rotors [10].

On the range $\Omega = [2, 4.5]$, the unbalance response (with $E = 5 \times 10^{-4}$, in this case) follows an analogous trend. Quasi-periodic regimes of increasing amplitude develop from a NS bifurcation as per Fig. 4, but find their amplitudes limited by contacts for $\Omega \geq 3.148$. As before, a new frequency component related to contact appears on the upper branch; thus, three-frequency quasi-periodic regimes are established. A comparison of free and forced responses, at $\Omega = 3.5$, is presented in Fig. 10.

The quasi-periodic nature of responses is evident from the torus-like trajectories in Fig. 10.a). From the perspective of radial displacement R, as in Fig. 10.b), the two-frequency response of the balanced rotor

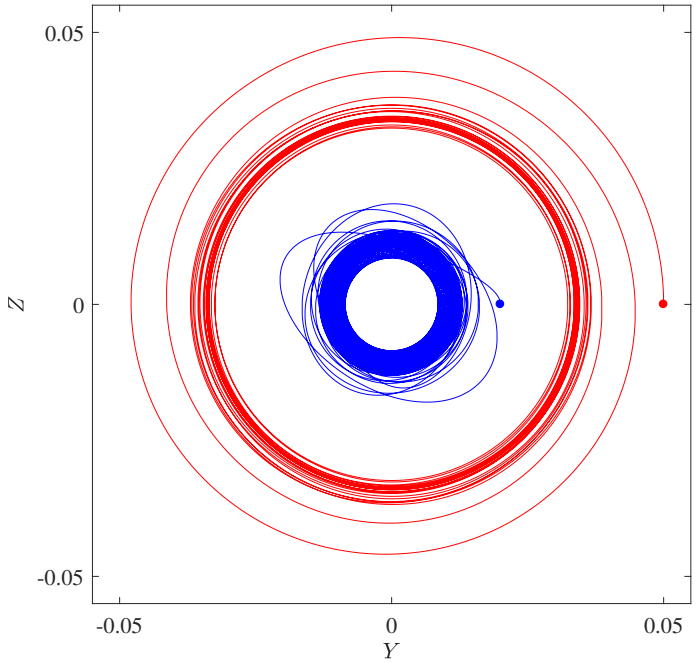

Figure 8: Rotor trajectory at point **A** for initial conditions $(Y_0, \dot{Y}_0, Z_0, \dot{Z}_0) = (0.05, 0, 0, 0.018)$ and $(Y_0, \dot{Y}_0, Z_0, \dot{Z}_0) = (0.02, 0, 0, 0.01)$, with the former leading to a periodic cycle (——) and the latter to a quasi-periodic response (——).

appears as a periodic oscillation about a constant-amplitude cycle. On the other hand, these oscillations are non-periodic for the unbalance response. Indeed, the associated power spectrum of Fig. 10.c) shows proof of a rich frequency content, with numerous components besides the underlying cycle represented by a peak at zero frequency. Hence, while the presence of a support has the positive effect of bounding the response amplitudes in the super-critical regime following a Hopf or NS bifurcation, this comes with a strongly nonlinear behaviour with potentially many overtones and several incommensurate frequencies.

5.2. Influence of friction coefficient

It has been reported in [9] that some quasi-periodic bouncing regimes in rubbing rotors are highly dependent on friction, whereas others are not. The influence of the friction coefficient μ is then worth investigated in more details on the nonlinear model under consideration.

Let consider the free rotor response at the values $(\Omega, \mu) = (3.5, 0.3)$, for which contact quasi-periodic motions are established (see Fig. 9). Periodic solution continuation indicates an unstable cycle at this point, whose Floquet exponents include a complex conjugate pair with positive real parts. Fixing Ω and following

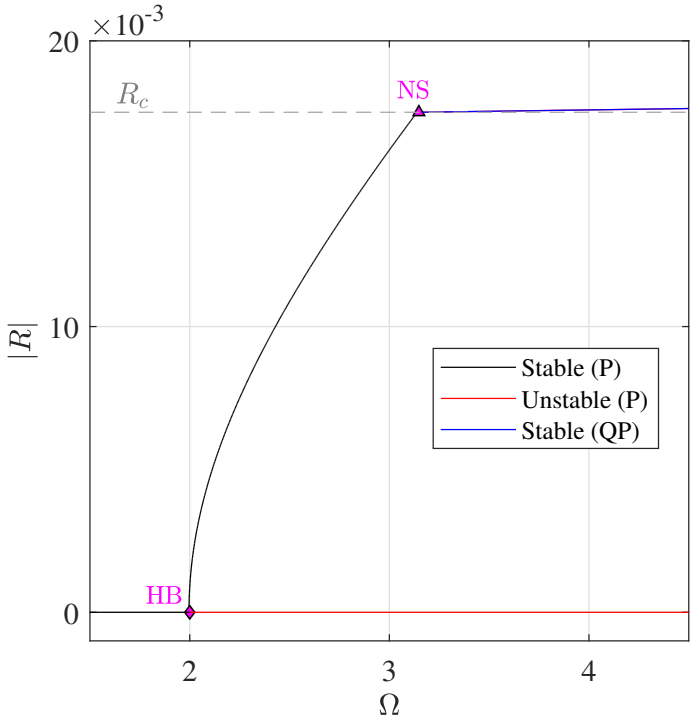

Figure 9: Free response of constrained rotor, where: $\mu = 0.3$, $\Omega_c^2 = 50$.

the solution branch (see Sect. 3) along decreasing values of μ from this initial point, the non-trivial exponents describe the curves shown in Fig. 11. A NS bifurcation occurs at $\mu_{\mathrm{NS}} = 0.0923$, which is thus the minimal value required to induce quasi-periodic motions at this rotation speed. In the vicinity of the bifurcation, these cycles contain a frequency component close to η_{NS}, the imaginary part of the corresponding unstable eigenvalue. This brief study reveals that, in the present case, quasi-periodic motions could be avoided if desired, by decreasing the friction coefficient through any adequate means of lubrication.

6. Conclusion

The Jeffcott rotor with geometrical nonlinearities and internal damping studied in this paper revealed a supercritical Hopf bifurcation leading to a limit cycle, for which a simple-form analytical solution was obtained. Results agreed with numerical simulations obtained with both a continuation algorithm and numerical time integration. The former of these, moreover, included a novel algorithm for switching from a periodic to a quasi-periodic solution branch at a Neimark-Sacker bifurcation. A very good correlation is

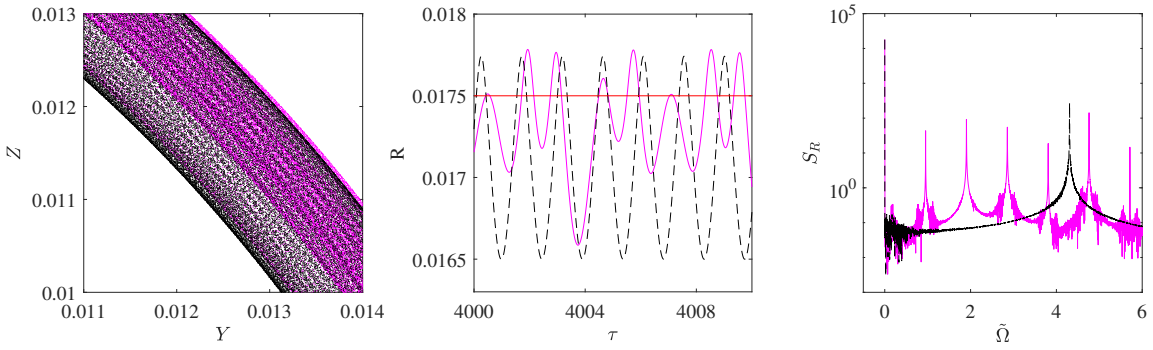

Figure 10: Rotor response at fixed frequency $\Omega = 3.5$ (contact): a) rotor trajectory, b) time history of radial displacement $R(\tau)$, and c) associated power spectra. Forced ($E = 5 \times 10^{-4}$) and free responses are represented by solid magenta (——) and dotted black (- - -) lines, respectively. Stator location R_c is represented by a horizontal line in b).

found that justified the third-order approximation and (quasi-)periodic assumption.

The post-bifurcation limit cycle can however be easily mistaken in experiments with external resonance excited by unbalance and those can be only distinguished with the mode speed. The linear unbalanced response rotates at rotor speed whereas the limit cycle does not. The study of this limit cycle shows that its radius can be small if the shaft is long, and its appearance may be postponed by designing significant external damping in comparison with internal damping.

The question of the experimental identification of instabilities due to internal damping [23, 24, 25] as well as the appropriate model for internal damping (viscous, hysteretic, or other) [3, 4, 26, 27] remains complex. Generally, the appearance of instability is catastrophic for the test bench. The first practical result is that it would be possible to measure the onset of the limit cycle on long shafts using pinned-ends conditions generating nonlinear stiffening and guaranteeing the integrity of the system.

With the use of advanced numerical methods that include bifurcation tracking and computation of quasi-periodic limit cycles, it was found that increasing the angular speed of an unbalanced rotor past the stability threshold of the balanced one leads to two-frequency quasi-periodic motions whose spectra consists of angular speed and the frequency of the underlying limit cycle. In such cases, there is a Neimark-Sacker rather than a Hopf bifurcation. The second practical result is that preserving the rotor integrity above the NS bifurcation necessitates to constrain the transverse displacement of the shaft. Simulations on the bounded rotor have shown that strongly nonlinear regimes develop as rotor stator contacts begins. Limit cycles of the balanced rotor become quasi-periodic in the presence of friction, in accordance with previous studies [9, 28], as

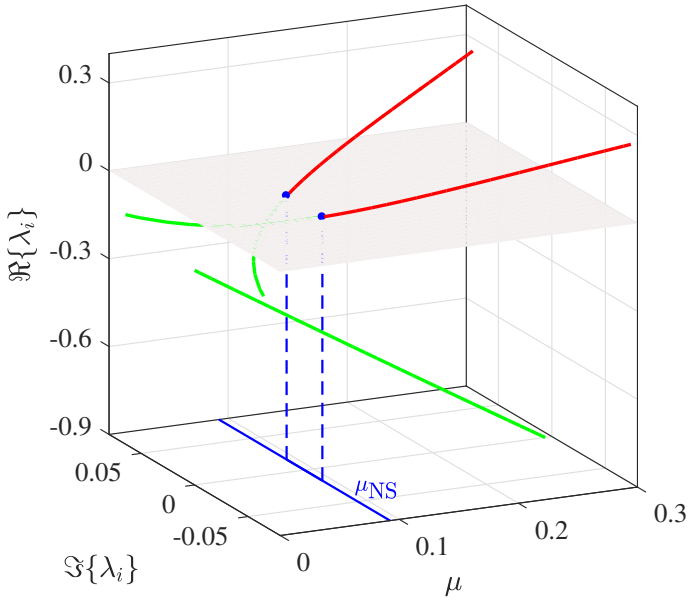

Figure 11: Floquet exponent dependence on μ, with $\Omega = 3.2$. NS bifurcation occurs at critical value $\mu_{\mathrm{NS}} = 0.0923$.

a new and friction-dependent frequency is born from contact. Similarly, limit cycles of bounded unbalanced rotor are three-frequency quasi-periodic. Bifurcation tracking yields a minimal value of friction coefficient leading to such regimes. The third practical result of this study is then that it may be possible to constrain the transverse displacement while avoiding a quasi-periodic regime by using lubricated enough rotor-stator interfaces.

Acknowledgement

The authors are grateful for the financial support of the French Defense Innovation Agency (AID).

References

[1] A. Tondl, Some Problems of Rotor Dynamics, Chapman & Hall, 1965.

[2] G. Genta, Dynamics of Rotating Systems, 2nd Edition, Springer, New-York, 2005.

[3] O. Montagnier, C. Hochard, Dynamic instability of supercritical driveshafts mounted on dissipative supports – effect of viscous and hysteretic internal damping, J Sound Vib 305 (2007) 378–400. doi:10.1016/j.jsv.2007.03.061.

[4] O. Montagnier, C. Hochard, Dynamics of a supercritical composite shaft mounted on viscoelastic supports, J Sound Vib 333 (2) (2014) 470–484. doi:10.1016/j.jsv.2013.09.021.

[5] G. Genta, C. Delprete, A. Tonoli, R. Vadori, Conditions for noncircular whirling of nonlinear isotropic rotors, Nonlinear Dyn 4 (2) (1993) 153–181. doi:10.1007/BF00045252.

[6] S. Bäuerle, R. Fiedler, H. Hetzler, An engineering perspective on the numerics of quasi-periodic oscillations, Nonlinear Dyn 108 (4) (2022) 3927–3950. doi:10.1007/s11071-022-07407-5.

[7] A. Batailly, M. Legrand, A. Millecamps, F. Garcin, Numerical-experimental comparison in the simulation of rotor/stator interaction through blade-tip/abradable coating contact, J Eng Gas Turbines Power 134 (8) (2012). doi:10.1115/1.4006446.

[8] C.-M. Liao, B. Balachandran, M. Karkoub, Y. L. Abdel-Magid, Drill-String Dynamics: Reduced-Order Models and Experimental Studies, J Vib Acoust 133 (4), 041008 (04 2011). doi:10.1115/1.4003406.

[9] E. Chipato, A. Shaw, M. Friswell, Frictional effects on the nonlinear dynamics of an overhung rotor, Commun Nonlinear Sci 78 (2019) 104875. doi:10.1016/j.cnsns.2019.104875.

[10] E. T. Chipato, A. D. Shaw, M. I. Friswell, R. Sánchez Crespo, Experimental study of rotor-stator contact cycles, J Sound Vib 502 (2021) 116097. doi:10.1016/j.jsv.2021.116097.

[11] G. V. Groll, D. Ewins, The harmonic balance method with arc-length continuation in rotor/stator contact problems, J Sound Vib 241 (2) (2001) 223–233. doi:10.1006/jsvi.2000.3298.

[12] N. Vlajic, A. R. Champneys, B. Balachandran, Nonlinear dynamics of a jeffcott rotor with torsional deformations and rotor-stator contact, Int J Non Linear Mech 92 (2017) 102–110. doi:10.1016/j.ijnonlinmec.2017.02.002.

[13] R. Seydel, Practical Bifurcation and Stability Analysis, Springer, 2010.

[14] T. M. Cameron, J. H. Griffin, An alternating frequency/time domain method for calculating the steady-state response of nonlinear dynamic systems, Journal of Applied Mechanics, ASME 56 (1) (1989) 149–154. doi:10.1115/1.3176036.

[15] L. Xie, S. Baguet, B. Prabel, R. Dufour, Bifurcation tracking by harmonic balance method for performance tuning of nonlinear dynamical systems, Mech Syst Sig Process 88 (2017) 445–461. doi:10.1016/j.ymssp.2016.09.037.

[16] R. Alcorta, S. Baguet, B. Prabel, P. Piteau, G. Jacquet-Richardet, Period doubling bifurcation analysis and isolated sub-harmonic resonances in an oscillator with asymmetric clearances, Nonlinear Dynamics 98 (4) (2019) 2939–2960. doi:10.1007/s11071-019-05245-6.

[17] N. Di Palma, B. Chouvion, F. Thouverez, Parametric study on internal resonances for a simplified nonlinear blade model, Int J Non Linear Mech 141 (9) (2022) 103941. doi:10.1016/j.ijnonlinmec.2022.103941.

[18] S. Quaegebeur, N. Di Palma, B. Chouvion, F. Thouverez, Exploiting internal resonances in nonlinear structures with cyclic symmetry as a mean of passive vibration control, Mech Syst Sig Process 178 (2022) 109232. doi:10.1016/j.ymssp.2022.109232.

[19] E. Doedel, H. B. Keller, J. P. Kernevez, Numerical analysis and control of bifurcation problems(i): bifurcation in finite dimensions, Int J Bifurcation Chaos 01 (03) (1991) 493–520. doi:10.1142/s0218127491000397.

[20] M. Guskov, F. Thouverez, Harmonic balance-based approach for quasi-periodic motions and stability analysis, J Vib Acoust 134 (3) (2012) 031003. doi:10.1115/1.4005823.

[21] J. S. Hesthaven, S. Gottlieb, D. Gottlieb, Spectral Methods for Time-Dependent Problems, Cambridge University Press, 2009.

[22] B. Chouvion, A wave approach to show the existence of detached resonant curves in the frequency response of a beam with an attached nonlinear energy sink, Mech Res Commun 95 (2019) 16–22. doi:10.1016/j.mechrescom.2018.11.006.

[23] O. Montagnier, C. Hochard, Experimental investigation of dynamic instability of supercritical driveshafts due to internal damping, in: Proceedings of the 7th IFToMM – Conference on Rotor Dynamics, Vienna, Austria, 2006.

[24] R. Sino, E. Chatelet, O. Montagnier, G. Jacquet-Richardet, Dynamic instability analysis of internally damped rotors, in: Proceedings of the ASME Turbo Expo 2007, Montreal, Canada, 2007. doi:10.1115/GT2007-27073.

[25] D. Roy, R.Tiwari, Experimental identification of internal and external damping in a rotor system with a fatigue-crack using full spectrum, Exp Tech 44 (2020) 509–528. doi:10.1007/s40799-020-00368-7.

[26] H. L. Wettergren, On the behavior of material damping due to multi-frequency excitation, J Sound Vib 206 (5) (1997) 725–735. doi:10.1006/jsvi.1997.1149.

[27] G. Genta, On a persistent misunderstanding of the role of hysteretic damping in rotordynamics, J Vib Acoust 126 (3) (2004) 459–461. doi:10.1115/1.1759694.

[28] A. D. Shaw, A. R. Champneys, M. I. Friswell, Normal form analysis of bouncing cycles in isotropic rotor stator contact problems, Int J Mech Sci 155 (2019) 83–97. doi:10.1016/j.ijmecsci.2019.02.035.